

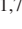


Localization of Chiral Edge States by the Non-Hermitian Skin Effect

Gui-Geng Liu (刘癸庚)^{1,*}, Subhaskar Mandal,^{1,*} Peiheng Zhou,^{2,*} Xiang Xi,^{3,*} Rimi Banerjee,¹
Yuan-Hang Hu,² Mingguai Wei,¹ Maoren Wang,² Qiang Wang,⁴ Zhen Gao⁵, Hongsheng Chen,⁶
Yihao Yang,^{6,†} Yidong Chong,^{1,7,‡} and Baile Zhang^{1,7,§}

¹*Division of Physics and Applied Physics, School of Physical and Mathematical Sciences, Nanyang Technological University, 21 Nanyang Link, Singapore 637371, Singapore*

²*National Engineering Research Center of Electromagnetic Radiation Control Materials, State Key Laboratory of Electronic Thin Film and Integrated Devices, University of Electronic Science and Technology of China, Chengdu 610054, China*


³*School of Electrical Engineering and Intelligentization, Dongguan University of Technology, Dongguan 523808, China*

⁴*School of Physics, Collaborative Innovation Center of Advanced Microstructures, Nanjing University, Nanjing, Jiangsu 210093, China*

⁵*Department of Electrical and Electronic Engineering, Southern University of Science and Technology, Shenzhen 518055, China*

⁶*Interdisciplinary Center for Quantum Information, State Key Laboratory of Modern Optical Instrumentation, ZJU-Hangzhou Global Science and Technology Innovation Center, College of Information Science and Electronic Engineering, Key Laboratory of Advanced Micro/Nano Electronic Devices and Smart Systems of Zhejiang, ZJU-UIUC Institute, Zhejiang University, Hangzhou 310027, China*

⁷*Centre for Disruptive Photonic Technologies, The Photonics Institute, Nanyang Technological University, 50 Nanyang Avenue, Singapore 639798, Singapore*

 (Received 28 May 2023; revised 9 December 2023; accepted 9 February 2024; published 12 March 2024)

Quantum Hall systems host chiral edge states extending along the one-dimensional boundary of any two-dimensional sample. In solid state materials, the edge states serve as perfectly robust transport channels that produce a quantized Hall conductance; due to their chirality, and the topological protection by the Chern number of the bulk band structure, they cannot be spatially localized by defects or disorder. Here, we show experimentally that the chiral edge states of a lossy quantum Hall system can be localized. In a gyromagnetic photonic crystal exhibiting the quantum Hall topological phase, an appropriately structured loss configuration imparts the edge states' complex energy spectrum with a feature known as point-gap winding. This intrinsically non-Hermitian topological invariant is distinct from the Chern number invariant of the bulk (which remains intact) and induces mode localization via the “non-Hermitian skin effect.” The interplay of the two topological phenomena—the Chern number and point-gap winding—gives rise to a non-Hermitian generalization of the paradigmatic Chern-type bulk-boundary correspondence principle. Compared to previous realizations of the non-Hermitian skin effect, the skin modes in this system have superior robustness against local defects and disorders.

DOI: [10.1103/PhysRevLett.132.113802](https://doi.org/10.1103/PhysRevLett.132.113802)

The significance of band topology was first discovered in the context of the quantum Hall effect in the 1980s [1]. In certain two-dimensional (2D) materials with broken time-reversal symmetry, the Hall conductance is exactly quantized, which is intimately tied to the fact that the bulk is insulating and charge transport occurs exclusively via chiral edge states [2]. The existence of the chiral edge states is guaranteed by the bulk bands' nontrivial topology, as characterized by a topological invariant [the Chern number C [3–5]; see Fig. 1(a)]. It is important for the quantum Hall effect that the chiral edge states are immune to backscattering (so long as the bulk is insulating), and hence do not undergo Anderson localization despite being one-dimensional (1D) transport channels. The robustness of chiral edge states against localization has even been directly observed in classical wave

realizations of quantum Hall systems, based on photonic [6,7], acoustic [8,9], and mechanical lattices [10].

Theories of band topology have mostly been developed in the context of quantum Hall phases, and other topological phases of matter that are all Hermitian (energy-conserving). In recent years, however, there has been a great deal of progress in understanding the topology of non-Hermitian materials [11–16]. Some concepts from Hermitian band topology, including the Chern number [12], turn out to be generalizable to the non-Hermitian regime. Moreover, non-Hermitian systems have been found to possess unique forms of band topology with no counterpart in the Hermitian regime. For instance, non-Hermitian band spectra may exhibit “point gaps,” defined by points in the complex plane that are encircled by but do not overlap with any band frequency (energy) [13,15]. (This is

distinct from a “line gap,” an arbitrary line in the complex plane separating the bands, which is the more straightforward generalization of the Hermitian notion of a band gap.) A point-gapped non-Hermitian Hamiltonian cannot be continuously deformed to a Hermitian Hamiltonian without closing the point gap. A point gap can be associated with an integer winding number, and nonzero windings are associated with the “non-Hermitian skin effect” (NHSE) [17–49], whereby an extensive number of bulk states become localized to a boundary. This phenomenon has been observed in recent experiments based on classical-wave systems [39–49]. To our knowledge, the implications of the NHSE for chiral edge states, which involve the interplay between point-gap topology and Chern number topology [35–37], have never been studied in any experiment.

In this Letter, we report on the observation of NHSE-induced localization of chiral edge states in a gyromagnetic photonic crystal (PhC). Such PhCs are commonly known as photonic topological insulators and exhibit photonic band gaps with nonzero Chern numbers [6]. By intentionally introducing losses to the system (thereby making it non-Hermitian) in a particular spatial pattern, we induce point gaps in the complex spectrum of the chiral edge states, with a pair of winding numbers (ν_x, ν_y) associated with the x and y directions respectively [see Fig. 1(b)]. We show that the point-gap winding topology determines whether the chiral edge states are localized along a 1D sample edge (when $\nu_x \neq 0$ or $\nu_y \neq 0$), or at a zero-dimensional (0D) corner (when both $\nu_x \neq 0$ and $\nu_y \neq 0$). The chiral edge states are thus governed by a hybrid invariant $(C; \nu_x, \nu_y)$ involving both point-gap and Chern number topology (see Fig. S1 for an illustration of the hybrid bulk-boundary correspondence [50]).

Our system also behaves differently from other NHSE realizations that are not based on chiral edge states [38–49]. Most of the theoretical models exhibiting the NHSE, such as the Hatano-Nelson model [13], are based on discrete (tight-binding) lattices, and the most common route to manifesting the NHSE is to introduce asymmetric couplings between discrete lattice sites, which have different magnitudes in the forward and backward directions

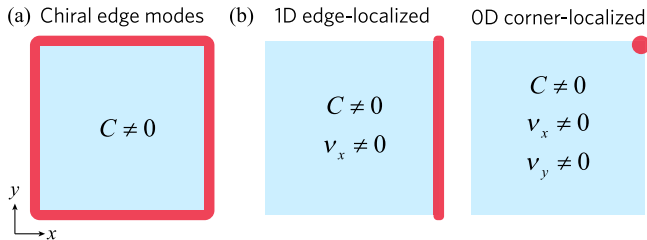


FIG. 1. Chern-type bulk-boundary correspondence and its non-Hermitian generalization. (a) Chiral edge states. (b) Edge- or corner-localized chiral edge states. The determination of boundary modes requires a hybrid topological invariant $(C; \nu_x, \nu_y)$.

(this determines the direction in which waves are “funneled” [39], and consequently where the skin modes are localized [16]). Our gyromagnetic PhC is continuous rather than discrete, and does not require asymmetric couplings, which have been challenging to implement on many experimental platforms. Moreover, because the skin effect in our system is based on chiral edge states, forward and backward transport is spatially separated (on opposite edges of a strip), providing the skin effect with superior robustness against local defects and disorder.

The PhC hosting localized chiral edge modes is depicted in Fig. 2(a). It consists of a square lattice with three gyromagnetic rods per unit cell, with each rod surrounded by microwave-absorbing materials with a relative permittivity of either $\epsilon_1 = \epsilon'_1 - i\epsilon''_1$ or $\epsilon_2 = \epsilon'_2 - i\epsilon''_2$, where $\epsilon'_1 \approx \epsilon'_2$ and $\epsilon''_1 \ll \epsilon''_2$ [50]. In the limit $\epsilon''_1 = \epsilon''_2 = 0$ and without losses in the gyromagnetic rods, the PhC would be

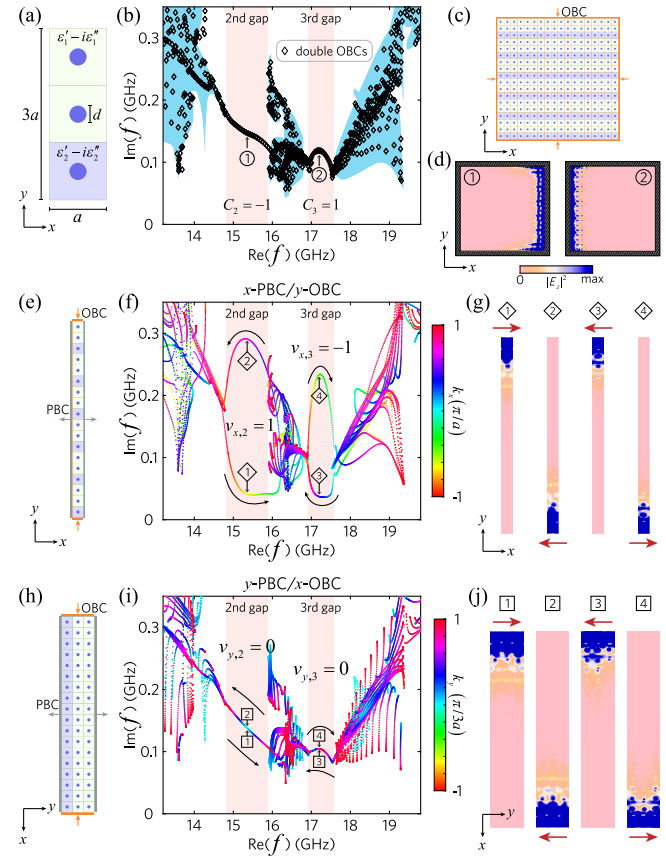


FIG. 2. First-principles study of edge-localized chiral edge states. (a) Unit cell of the PhC. $a = 10$ mm and $d = 3$ mm. (b) Eigenfrequencies for double-PBCs (blue region) and double-OBCs (rhombic dots). (c) Finite structure with double-OBCs. (d) Eigenfunctions for states labeled “1” and “2” in (b). (e) Supercell with x -PBC/ y -OBC. (f, g) Eigenfrequencies and eigenfunctions for the supercell in (e). The black arrows in (f) denote the k_x increasing directions. The red arrows in (g) indicate the group velocities of the edge states. (h)–(j) Similar to (e)–(g) but for y -PBC/ x -OBC.

Hermitian and all eigenfrequencies would be real. The unit cell is mirror symmetric along the x direction, but not along y . We apply a static magnetic field of 0.7 T along the z axis, breaking time-reversal symmetry in the gyromagnetic rods [50]. The PhC is placed in a parallel-plate waveguide, and we focus on the transverse magnetic modes, which have electric fields polarized along the z axis.

Because of the material losses, the PhC is non-Hermitian. Its bulk band spectrum, calculated from a single unit cell under periodic boundary conditions (PBCs) along both x and y (“double-PBCs”), forms a set of distinct complex bands each filling a bounded region of the complex frequency plane, as indicated by the blue areas in Fig. 2(b). The bands are thus separated by line gaps. For the second and third gaps, depicted in this plot, the non-Hermitian generalization of the Chern number is well-defined [12] and yields $C_2 = -1$ and $C_3 = 1$ [50].

Next, we consider a finite-size sample of the PhC, bounded by copper claddings along both the x and y directions, as shown in Fig. 2(c). Because the claddings act as perfect reflectors at microwave frequencies, this configuration is equivalent to open boundary conditions (OBCs) in a tight-binding model (i.e., open truncation of the lattice) along both x and y (“double-OBCs”). The calculated complex eigenfrequencies are plotted as diamond markers in Fig. 2(b). We observe that a large set of eigenfrequencies, corresponding to bulk modes, occupy the same areas as the bulk band frequencies. However, there are also eigenfrequencies spanning the bulk line gaps; the corresponding eigenfunctions are strongly localized along the sample’s right edge (for gap 2) or left edge (for gap 3), as shown by the two exemplary states plotted in Fig. 2(d).

The existence of these edge states, which are localized to part of the sample boundary, arises jointly from point-gap winding (an intrinsically non-Hermitian topological invariant) and the Chern number (a topological band invariant generalized from the Hermitian regime). To demonstrate the former, we study the supercell depicted in Fig. 2(e), which has PBCs along x and OBCs in the y direction (“ x -PBC/ y -OBC”). The calculated eigenfrequencies, plotted in Fig. 2(f), form a spectral loop in each gap. As the wave number k_x sweeps through the 1D Brillouin zone of the supercell, the eigenfrequencies in the second (third) gap advance anticlockwise (clockwise), producing a point-gap winding number of $+1$ (-1). This gives rise to the NHSE [25] and the localization behavior in the double-OBCs sample discussed in the previous paragraph.

Next, we plot intensity distributions for the supercell eigenstates in the bulk gap [Fig. 2(g)]. The edge states are chiral: states of opposite k_x lie on opposite (upper or lower) edges of the supercell, consistent with the bulk non-Hermitian Chern number of each gap. Moreover, the states on the upper (lower) arm of each spectral loop, whose eigenfrequencies have a larger (smaller) imaginary part, lie on the lower (upper) edge of the supercell. This can be

understood intuitively from the supercell’s configuration: the states on the lower edge [e.g., states 2 and 4 in Fig. 2(g)] travel through a lossier region than those on the upper edge [states 1 and 3 in Fig. 2(g)].

The point-gap winding of the PhC can be quantified using the winding numbers [25]

$$\nu_{\alpha,n} = \oint_{BZ} \frac{dk_{\alpha}}{2\pi i} \frac{d}{dk_{\alpha}} \ln(f(k_{\alpha}) - f_0), \quad (1)$$

where $\alpha = x, y$ indicates the direction along which PBCs are imposed on a supercell, n is the gap index, f is the complex eigenfrequency, and f_0 is a reference frequency within the loop. As previously noted, $\nu_{x,2} = 1$ and $\nu_{x,3} = -1$; the sign difference between the two point-gap windings is consistent with the edge states being localized on opposite sides of the double-OBCs sample, as seen in Fig. 2(d) [50]. Similarly, we can construct a supercell along x (y -PBC/ x -OBC), as depicted in Fig. 2(h). In this case, we do not observe any spectral loops [Figs. 2(i) and 2(j)], so $\nu_{y,2} = 0$ and $\nu_{y,3} = 0$ and the NHSE does not occur. This is consistent with the lack of localization on the upper and lower edges in the double-OBCs system [Fig. 2(d)] [25].

Next, we fabricate the sample shown in Figs. 3(a) and 3(b), and characterize it using multiple “pump-probe” microwave measurements on it. In order to determine the spatial profiles of the non-Hermitian PhC’s eigenstates, we utilize the principle that a spatially structured source preferentially excites eigenstates with matching spatial intensity profiles. We thus consider a line source (i.e., an array of dipole sources) placed along either the right or left edge of the sample, as indicated respectively by the cyan and magenta stars in Fig. 3(a). The spatial profiles of these

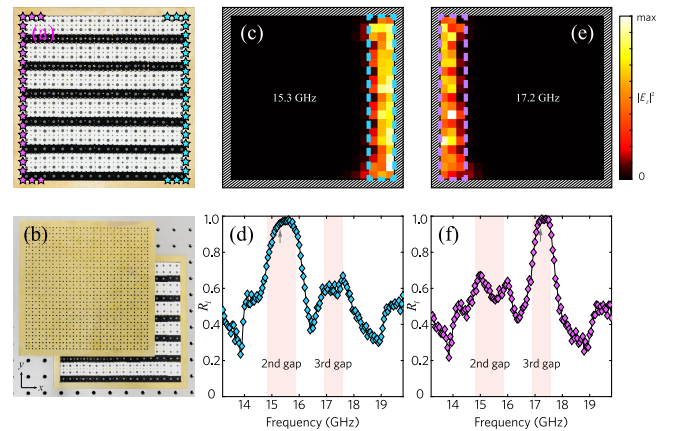


FIG. 3. Observation of edge-localized chiral edge states. (a),(b) Photograph of the fabricated PhC with top copper plate removed (a) and shifted (b) for clear visualization. (c),(e) Measured intensity distributions excited by a line source near the right or left boundary in (a), operating at frequencies of 15.3 GHz and 17.2 GHz, respectively. (d),(f) Measured ratios of edge-localized energy. The arrows point to 15.3 GHz in (d) and 17.2 GHz in (f).

line sources respectively match the edge states for the second and third gaps, as shown in Fig. 2(d). We experimentally measure the fields produced by each constituent dipole source, and map out the intensity distribution induced by the entire line source. The results are shown in Figs. 3(c) and 3(e) for two different frequencies in the second and third gaps (see Supplemental Material for more details about the excitation of the line source [50]).

Figure 3(c) shows the measured intensity distribution for a line source on the right boundary [cyan stars in Fig. 3(a)] at a frequency of 15.3 GHz (in gap 2). The intensity is uniformly distributed along the right boundary, matching both the profile of the line source and the predicted profile of the eigenstate at this frequency [Fig. 2(d)]. For comparison, we also verified that for other choices of source profiles, the resulting intensity profile does not match the source profile (see Fig. S3 [50]). To quantify the degree of localization of the measured intensity profile, we define

$$R_l = \frac{\int_{\Pi_s} |E_z|^2 dx dy}{\int_{\Pi} |E_z|^2 dx dy}, \quad (2)$$

where $|E_z|^2$ is the electric field intensity excited by the line source, Π denotes the entire area of the sample, and Π_s denotes the area covering the rightmost unit cells in the sample [encircled by the cyan dashed line in Fig. 3(c)]. A larger value of R_l indicates that the fields are more strongly localized near the right boundary. Figure 3(d) plots the measured R_l versus frequency. We see that R_l exhibits a prominent peak around 15.3 GHz, coincident with gap 2, and takes on lower values at other frequencies. These results confirm the prediction that the edge states in gap 2 are localized along the right boundary, in accordance with the point-gap winding $\nu_{x,2} = 1$ and $\nu_{y,2} = 0$.

Similarly, when the line source is placed at the left boundary [magenta stars in Fig. 3(a)], the measured intensity profile at 17.2 GHz is strongly localized along the left boundary, as shown in Fig. 3(e). Using a localization measure R_l , defined similarly to Eq. (2) but singling out the leftmost unit cells, we find that the localization is enhanced at frequencies coinciding with gap 3, as shown in Fig. 3(f). These results are again consistent with the theoretical predictions [Fig. 2(d)]. Results for other choices of source profile can be found in Fig. S4 [50].

By adjusting the design of the PhC, we can induce different point-gap winding numbers, so that the NHSE manifests differently. Figure 4(a) shows a PhC unit cell with broken mirror symmetry in both the x and y directions. The bulk spectrum (double-PBCs) is similar to the previous case, with clear line gaps. To determine the point-gap windings, we take supercells with x -PBC/ y -OBC [Fig. 4(c)] and y -PBC/ x -OBC [Fig. 4(d)]; these two cases give identical spectra [colored lines in Fig. 4(b)] containing loops in both gaps with $\nu_{x,2} = 1$, $\nu_{y,2} = 1$, $\nu_{x,3} = -1$, and $\nu_{y,3} = -1$. The NHSE is thus predicted to localize the chiral edge states toward both the $+x$ and $+y$ directions

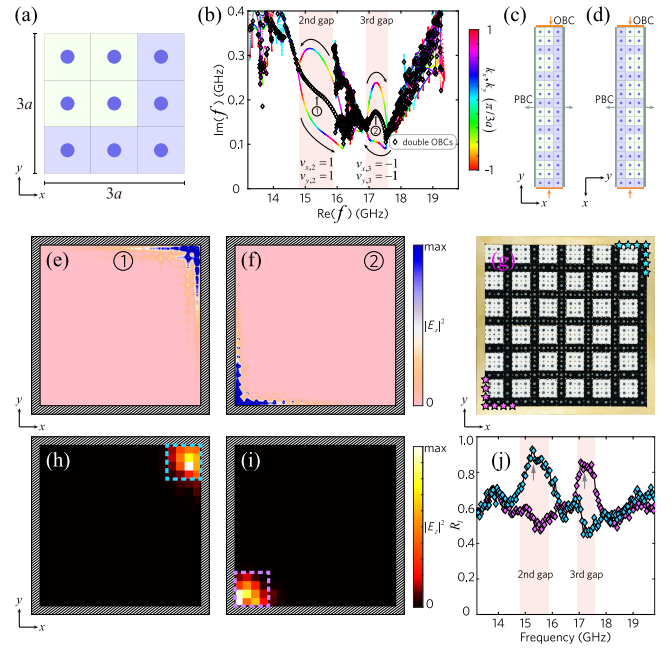


FIG. 4. Observation of corner-localized chiral edge states. (a) Unit cell of the PhC. (b) Colored lines: eigenfrequencies for the supercell in (c) under x -PBC/ y -OBC and (d) under y -PBC/ x -OBC. Rhombic dots: Eigenfrequencies for the sample under double-OBCs in (g). (e),(f) Eigenfunctions for the sample in (g). (h),(i) Measured intensity distributions excited by the corner source in (g). (j) Measured ratios of corner-localized energy. The arrows represent 15.3 GHz and 17.2 GHz.

in gap 2, and toward the $-x$ and $-y$ directions in gap 3. We then construct a finite sample under double-OBCs and plot its eigenfrequencies as diamond markers in Fig. 4(b). In this system, gaps 2 and 3 are found to be spanned by edge states, whose eigenfunctions are localized on the upper-right sample corner [Fig. 4(e) for gap 2] and lower-left sample corner [Fig. 4(f) for gap 3], respectively, consistent with predictions of the NHSE.

Next, we implement an experimental sample with the loss configuration described in the previous paragraph [see Fig. 4(g)]. The eigenstates are investigated using a procedure similar to what we have previously described; in this case, we implement corner sources consisting of the dipole sources indicated by cyan or magenta stars in Fig. 4(g), matching the spatial profiles of the simulated eigenstate in Figs. 4(e) and 4(f). The resulting measured intensity distributions are shown in Figs. 4(h) and 4(i), respectively (more measurement results, for other source profiles, are shown in Figs. S5–S7 [50]). In Fig. 4(j), we plot the spectral response of the energy localization near the two corners, defined by analogy to Eq. (2), with the singled-out regions Π_s now consisting of the cyan and magenta rectangles in Figs. 4(h) and 4(i), respectively. We thus conclude that the chiral edge states are strongly localized around the upper-right and lower-left corners at frequencies in gap 2 and gap 3, respectively, consistent with the predictions in Figs. 4(e) and 4(f).

The above results can be understood in terms of a bulk-boundary correspondence governed by a hybrid topological invariant

$$\nu_n = (C_n; \nu_{x,n}, \nu_{y,n}) \quad (3)$$

for each gap n . Only a combination of the Chern number and point-gap winding numbers can predict the existence and localization behavior of the edge states. The Chern number C_n determines the number of chiral edge states in the gap, while the two point-gap winding numbers determine how they are localized in the x and y directions [50]. In Fig. S8, we study the boundary modes in a gap with a large Chern number $C_n = 2$ and find two branches of localized chiral edge states spanning in the gap [50].

In conclusion, we have demonstrated the existence of edge and corner localized chiral edge states in a gyromagnetic PhC exhibiting the NHSE. The Chern-type bulk-boundary correspondence has been generalized to the non-Hermitian regime, for which we have proposed a hybrid topological invariant that incorporates both the Chern number and two winding numbers to accurately predict the boundary states in both Hermitian and non-Hermitian cases. Our Letter represents the first observation of the NHSE in a PhC, going beyond the tight-binding approximation [33]. Because of the role of the chiral edge states, the NHSE in this system exhibits superior robustness against local defects compared to previous NHSE realizations [50]. Our findings may find applications in lasing [52] and robust light harvesting [39].

This work was sponsored by the National Research Foundation Competitive Research Program No. NRF-CRP23-2019-0007. Work at University of Electronic Science and Technology of China was sponsored by the National Natural Science Foundation of China (NSFC) (No. 52022018 and No. 52021001). The work at Zhejiang University was sponsored by the Key Research and Development Program of the Ministry of Science and Technology under Grants No. 2022YFA1405200 (Y. Y.), No. 2022YFA1404704 (H. C.), and No. 2022YFA1404900 (Y. Y.), the National Natural Science Foundation of China (NNSFC) under Grants No. 11961141010 (H. C.), No. 62175215 (Y. Y.), and No. 61975176 (H. C.), the Fundamental Research Funds for the Central Universities (2021FZZX001-19) (Y. Y.), and the Excellent Young Scientists Fund Program (Overseas) of China (Y. Y.). The work at Southern University of Science and Technology was sponsored by the National Natural Science Foundation of China (No. 62375118, No. 6231101016, and No. 12104211).

*These authors contributed equally to this work.

†Corresponding author: yangyihao@zju.edu.cn

‡Corresponding author: yidong@ntu.edu.sg

§Corresponding author: blzhang@ntu.edu.sg

[1] K. von Klitzing *et al.*, 40 years of the quantum Hall effect, *Nat. Rev. Phys.* **2**, 397 (2020).

- [2] B. I. Halperin, Quantized Hall conductance, Current-carrying edge states, and the existence of extended states in a two-dimensional disordered potential, *Phys. Rev. B* **25**, 2185 (1982).
- [3] D. J. Thouless, M. Kohmoto, M. P. Nightingale, and M. den Nijs, Quantized Hall conductance in a two-dimensional periodic potential, *Phys. Rev. Lett.* **49**, 405 (1982).
- [4] M. Z. Hasan and C. L. Kane, Colloquium: Topological insulators, *Rev. Mod. Phys.* **82**, 3045 (2010).
- [5] X.-L. Qi and S.-C. Zhang, Topological insulators and superconductors, *Rev. Mod. Phys.* **83**, 1057 (2011).
- [6] Z. Wang, Y. Chong, J. D. Joannopoulos, and M. Soljačić, Observation of unidirectional backscattering-immune topological electromagnetic states, *Nature (London)* **461**, 772 (2009).
- [7] M. Hafezi, S. Mittal, J. Fan, A. Migdall, and J. M. Taylor, Imaging topological edge states in silicon photonics, *Nat. Photonics* **7**, 1001 (2013).
- [8] Z. Yang, F. Gao, X. Shi, X. Lin, Z. Gao, Y. Chong, and B. Zhang, Topological acoustics, *Phys. Rev. Lett.* **114**, 114301 (2015).
- [9] Y. Ding, Y. Peng, Y. Zhu, X. Fan, J. Yang, B. Liang, X. Zhu, X. Wan, and J. Cheng, Experimental demonstration of acoustic Chern insulators, *Phys. Rev. Lett.* **122**, 014302 (2019).
- [10] L. M. Nash, D. Kleckner, A. Read, V. Vitelli, A. M. Turner, and W. T. M. Irvine, Topological mechanics of gyroscopic metamaterials, *Proc. Natl. Acad. Sci. U.S.A.* **112**, 14495 (2015).
- [11] D. Leykam, K. Y. Bliokh, C. Huang, Y. D. Chong, and F. Nori, Edge modes, degeneracies, and topological numbers in non-Hermitian systems, *Phys. Rev. Lett.* **118**, 040401 (2017).
- [12] H. Shen, B. Zhen, and L. Fu, Topological band theory for non-Hermitian Hamiltonians, *Phys. Rev. Lett.* **120**, 146402 (2018).
- [13] Z. Gong, Y. Ashida, K. Kawabata, K. Takasan, S. Higashikawa, and M. Ueda, Topological phases of non-Hermitian systems, *Phys. Rev. X* **8**, 031079 (2018).
- [14] K. Kawabata, K. Shiozaki, M. Ueda, and M. Sato, Symmetry and topology in non-Hermitian physics, *Phys. Rev. X* **9**, 041015 (2019).
- [15] E. J. Bergholtz, J. C. Budich, and F. K. Kunst, Exceptional topology of non-Hermitian systems, *Rev. Mod. Phys.* **93**, 015005 (2021).
- [16] F. Song, S. Yao, and Z. Wang, Non-Hermitian topological invariants in real space, *Phys. Rev. Lett.* **123**, 246801 (2019).
- [17] T. E. Lee, Anomalous edge state in a non-Hermitian lattice, *Phys. Rev. Lett.* **116**, 133903 (2016).
- [18] F. K. Kunst, E. Edvardsson, J. C. Budich, and E. J. Bergholtz, Biorthogonal bulk-boundary correspondence in non-Hermitian systems, *Phys. Rev. Lett.* **121**, 026808 (2018).
- [19] S. Yao and Z. Wang, Edge states and topological invariants of non-Hermitian systems, *Phys. Rev. Lett.* **121**, 086803 (2018).
- [20] T. Liu, Y. R. Zhang, Q. Ai, Z. Gong, K. Kawabata, M. Ueda, and F. Nori, Second-order topological phases in non-Hermitian systems, *Phys. Rev. Lett.* **122**, 076801 (2019).

- [21] C. H. Lee, L. Li, and J. Gong, Hybrid higher-order skin-topological modes in nonreciprocal systems, *Phys. Rev. Lett.* **123**, 016805 (2019).
- [22] Y. Yi and Z. Yang, Non-Hermitian skin modes induced by on-site dissipations and chiral tunneling effect, *Phys. Rev. Lett.* **125**, 186802 (2020).
- [23] L. Li, C. H. Lee, and J. Gong, Topological switch for non-Hermitian skin effect in cold-atom systems with loss, *Phys. Rev. Lett.* **124**, 250402 (2020).
- [24] N. Okuma, K. Kawabata, K. Shiozaki, and M. Sato, Topological origin of non-Hermitian skin effects, *Phys. Rev. Lett.* **124**, 086801 (2020).
- [25] K. Zhang, Z. Yang, and C. Fang, Correspondence between winding numbers and skin modes in non-Hermitian systems, *Phys. Rev. Lett.* **125**, 126402 (2020).
- [26] D. S. Borgnia, A. J. Kruchkov, and R. J. Slager, Non-Hermitian boundary modes and topology, *Phys. Rev. Lett.* **124**, 056802 (2020).
- [27] S. Mandal, R. Banerjee, E. A. Ostrovskaya, and T. C. H. Liew, Nonreciprocal transport of exciton polaritons in a non-Hermitian chain, *Phys. Rev. Lett.* **125**, 123902 (2020).
- [28] L. Li, C. H. Lee, S. Mu, and J. Gong, Critical non-Hermitian skin effect, *Nat. Commun.* **11**, 5491 (2020).
- [29] S. Longhi, Non-Bloch-band collapse and chiral Zener tunneling, *Phys. Rev. Lett.* **124**, 066602 (2020).
- [30] K. Kawabata, M. Sato, and K. Shiozaki, Higher-order non-Hermitian skin effect, *Phys. Rev. B* **102**, 205118 (2020).
- [31] L. J. Lang, S. L. Zhu, and Y. D. Chong, Non-Hermitian topological end breathers, *Phys. Rev. B* **104**, L020303 (2021).
- [32] K. Zhang, Z. Yang, and C. Fang, Universal non-Hermitian skin effect in two and higher dimensions, *Nat. Commun.* **13**, 1 (2022).
- [33] J. Zhong, K. Wang, Y. Park, V. Asadchy, C. C. Wojcik, A. Dutt, and S. Fan, Nontrivial point-gap topology and non-Hermitian skin effect in photonic crystals, *Phys. Rev. B* **104**, 125416 (2021).
- [34] Y. X. Xiao and C. T. Chan, Topology in non-Hermitian Chern insulators with skin effect, *Phys. Rev. B* **105**, 075128 (2022).
- [35] Y. Li, C. Liang, C. Wang, C. Lu, and Y. C. Liu, Gain-loss-induced hybrid skin-topological effect, *Phys. Rev. Lett.* **128**, 223903 (2022).
- [36] W. Zhu and J. Gong, Hybrid skin-topological modes without asymmetric couplings, *Phys. Rev. B* **106**, 035425 (2022).
- [37] F. Schindler, K. Gu, B. Lian, and K. Kawabata, Hermitian bulk–non-Hermitian boundary correspondence, *PRX Quantum* **4**, 030315 (2023).
- [38] L. Xiao, T. Deng, K. Wang, G. Zhu, Z. Wang, W. Yi, and P. Xue, Non-Hermitian bulk–boundary correspondence in quantum dynamics, *Nat. Phys.* **16**, 761 (2020).
- [39] S. Weidemann, M. Kremer, T. Helbig, T. Hofmann, A. Stegmaier, M. Greiter, R. Thomale, and A. Szameit, Topological funneling of light, *Science* **368**, 311 (2020).
- [40] T. Helbig, T. Hofmann, S. Imhof, M. Abdelghany, T. Kiessling, L. W. Molenkamp, C. H. Lee, A. Szameit, M. Greiter, and R. Thomale, Generalized bulk–boundary correspondence in non-Hermitian topoelectrical circuits, *Nat. Phys.* **16**, 747 (2020).
- [41] T. Hofmann *et al.*, Reciprocal skin effect and its realization in a topoelectrical circuit, *Phys. Rev. Res.* **2**, 023265 (2020).
- [42] A. Ghatak, M. Brandenbourger, J. van Wezel, and C. Coullais, Observation of non-Hermitian topology and its bulk–edge correspondence in an active mechanical metamaterial, *Proc. Natl. Acad. Sci. U.S.A.* **117**, 29561 (2020).
- [43] K. Wang, A. Dutt, K. Y. Yang, C. C. Wojcik, J. Vučković, and S. Fan, Generating arbitrary topological windings of a non-Hermitian band, *Science* **371**, 1240 (2021).
- [44] L. S. Palacios, S. Tchoumakov, M. Guix, I. Pagonabarraga, S. Sánchez, and A. G. Grushin, Guided accumulation of active particles by topological design of a second-order skin effect, *Nat. Commun.* **12**, 4691 (2021).
- [45] X. Zhang, Y. Tian, J. H. Jiang, M. H. Lu, and Y. F. Chen, Observation of higher-order non-Hermitian skin effect, *Nat. Commun.* **12**, 5377 (2021).
- [46] L. Zhang *et al.*, Acoustic non-Hermitian skin effect from twisted winding topology, *Nat. Commun.* **12**, 6297 (2021).
- [47] D. Zou, T. Chen, W. He, J. Bao, C. H. Lee, H. Sun, and X. Zhang, Observation of hybrid higher-order skin-topological effect in non-Hermitian topoelectrical circuits, *Nat. Commun.* **12**, 7201 (2021).
- [48] Q. Liang, D. Xie, Z. Dong, H. Li, H. Li, B. Gadway, W. Yi, and B. Yan, Dynamic signatures of non-Hermitian skin effect and topology in ultracold atoms, *Phys. Rev. Lett.* **129**, 070401 (2022).
- [49] Y. G. Liu, Y. Wei, O. Hemmatyar, G. G. Pyrialakos, P. S. Jung, D. N. Christodoulides, and M. Khajavikhan, Complex skin modes in non-Hermitian coupled laser arrays, *Light* **11**, 1 (2022).
- [50] See Supplemental Material at <http://link.aps.org/supplemental/10.1103/PhysRevLett.132.113802> for calculation of Chern numbers for non-Hermitian PhCs, materials and experimental setup, numerical simulation, robustness of localized chiral edge states, calculation of winding number, excitation of dipole arrays, and other theoretical results and experimental data, which includes Ref. [51].
- [51] W. A. Benalcazar, B. A. Bernevig, and T. L. Hughes, Electric multipole moments, topological multipole moment pumping, and chiral hinge states in crystalline insulators, *Phys. Rev. B* **96**, 245115 (2017).
- [52] B. Bahari, A. Ndao, F. Vallini, A. E. Amili, Y. Fainman, and B. Kanté, Nonreciprocal lasing in topological cavities of arbitrary geometries, *Science* **358**, 636 (2017).